

# Sea ice kinematics and surface properties from RADARSAT synthetic aperture radar during the SHEBA drift

Harry L. Stern and Richard E. Moritz

Polar Science Center, Applied Physics Laboratory, University of Washington, Seattle, Washington, USA

Received 2 June 2000; revised 4 January 2001; accepted 12 September 2001; published 18 September 2002.

[1] Satellite data are important for providing the large-scale context of the Surface Heat Budget of the Arctic Ocean (SHEBA) station and for characterizing the spatial variability of the sea ice in its vicinity. The Canadian RADARSAT satellite collected 195 synthetic aperture radar (SAR) images of the SHEBA site over the course of the 1 year drift. The RADARSAT Geophysical Processor System (RGPS) used these images to compute the spatial pattern of ice motion within 100 km of the SHEBA station by tracking features in sequential images. From the ice motion data the divergence and shear of the pack ice are estimated. The divergence is large from November to January, followed by a gradual convergence from February through July. The character of the ice motion changes at the end of July, from piecewise rigid motion to free drift. The ice motion reverts to its winterlike character in late September. Thus the “kinematic” summer runs from late July to late September. The radar backscatter also goes through seasonal transitions, capturing the abrupt onset of melt (29 May) and freeze-up (15 August). The concentration of multiyear ice is about 94% in the fall, and its backscatter signature remains stable through spring. Multiyear and first-year ice cannot be distinguished during the summer melt season, when the mean backscatter is negatively correlated with the surface air temperature. The “thermodynamic” summer runs from late May to mid-August.

*INDEX TERMS:* 4207 Oceanography: General: Arctic and Antarctic oceanography; 4275 Oceanography: General: Remote sensing and electromagnetic processes (0689); 4540 Oceanography: Physical: Ice mechanics and air/sea/ice exchange processes; *KEYWORDS:* sea ice; synthetic aperture radar (SAR); SHEBA

**Citation:** Stern H. L., and R. E. Moritz, Sea ice kinematics and surface properties from RADARSAT synthetic aperture radar during the SHEBA drift, *J. Geophys. Res.*, 107(C10), 8028, doi:10.1029/2000JC000472, 2002.

## 1. Introduction

[2] One of the purposes of the Surface Heat Budget of the Arctic Ocean (SHEBA) drift phase, from October 1997 to October 1998, was to make measurements of the ocean, atmosphere, and sea ice properties that could then be used to improve parameterizations of processes in single-column models of Arctic air-sea-ice interaction. The ultimate goal is to “scale up” the single-column models and results to improve basin-wide simulations of Arctic climate and its interaction with the global climate [Moritz and Perovich, 1996]. Remote sensing data are essential for characterizing the local and basin-wide properties of the sea ice and their variability so that proper scaling up can be accomplished.

[3] This paper describes a unique remote sensing data set and two areas of application: sea ice motion and deformation, and the evolution of sea ice surface properties. The Canadian RADARSAT satellite collected 195 synthetic aperture radar (SAR) images of the SHEBA site between 1 November 1997 and 8 October 1998 or roughly one image every 1–3 days. The C band (5.3 GHz) RADARSAT SAR imaged a swath on the Earth 460 km wide (in ScanSAR mode) with a pixel size of 50 m, unhampered by clouds or darkness. The satellite data were received and processed into imagery at the Alaska SAR Facility (ASF) in Fairbanks. Sequential pairs of images were

then processed by the RADARSAT Geophysical Processor System (RGPS) at the Jet Propulsion Laboratory (JPL) in Pasadena to derive the motion of the sea ice on a 5 km grid by tracking common features in each pair of images. Thus we have a year-long record of the spatial pattern of ice motion and the radar backscatter in the vicinity of the SHEBA site.

[4] Animation of the sequence of images reveals for the first time the details of sea ice motion in time-lapse fashion. Large “plates” of ice (~100 km or more) are seen to slide past one another; leads open and new ice forms in them; leads close and bright pressure ridges appear; dramatic seasonal transitions are marked by large jumps in radar backscatter. These events have been seen before in isolation but not in a time series following a single location through a whole annual cycle.

[5] Several research projects are making use of this data set. Work is underway to relate the large-scale discontinuous plate motion to the continuous wind forcing [Moritz and Stern, 2001]. The ice motion computed by RGPS has been used to drive a granular model of sea ice [Hopkins, 1999]. The ice divergence computed from the RGPS ice motion grids has been used to drive a single-column ice thickness model [Curry *et al.*, 2001]. The strain rates have also been used in a study relating Arctic pack ice stress and deformation [Richter-Menge *et al.*, 2002] and in a study of rafting and redistribution of ice thickness [Babko, 2000]. The ice motion data are being used in a data fusion study to derive the best estimate of ice deformation near SHEBA [Lindsay, 2002]. Other potential applications

include the study of lead patterns, the testing of anisotropic constitutive models of sea ice [e.g., *Hibler and Schulson, 2000*], the investigation of the information content of SAR images [e.g., *Kerman et al., 1999*], and the comparisons with surface measurements that could correlate with changes in radar backscatter.

[6] After describing the data sets and derived products we present some results from the analysis of the ice deformation and the time series of radar backscatter. The kinematic and radiometric analyses reveal different regimes and seasonal transitions in the sea ice. The final section contains conclusions and remarks about other relevant RGPS data sets.

## 2. Data Sets

### 2.1. Imagery

[7] The frequent RADARSAT coverage of the SHEBA site is due to NASA's RGPS project. The data acquisition plan for RGPS calls for imaging the entire Arctic basin every 3 days. The total U.S. allocation for RADARSAT data is limited, but the SHEBA site fell within the domain of the RGPS acquisitions, so images were acquired regularly without additional planning by the SHEBA Project Office and without additional use of the U.S. allocation.

[8] The 195 images produced by ASF are geocoded to the Special Sensor Microwave Imager (SSM/I) polar stereographic projection, with standard parallel at 70°N latitude and +X axis along 45°E longitude. Included with the images are calibration coefficients that allow pixel values to be converted to normalized radar backscatter. The pixel size is 50 m, and each image is approximately 230 Mb in size.

[9] To reduce the size and complexity of the image data and enhance their usefulness, we first applied the calibration coefficients (with software from ASF) to convert pixel values to radar backscatter and then extracted two subimages from each calibrated image. Both subimages are centered on the SHEBA station. One is 40 × 40 km in extent and retains the original pixel size of 50 m; the other is 200 × 200 km in extent and has a pixel size of 250 m (5 × 5 block averaging and subsampling). The SHEBA station was identified in each original image by a manual procedure in which the known daily position of the ship was first used to display a subimage of the approximate station location. The operator then selected the exact pixel at the center of the station, which almost always showed up as a small bright (high backscatter) cluster of pixels. The manually selected pixel location became the center of the extracted subimages. Ensuring that the SHEBA station is at the center of each subimage allows the animated sequence of subimages to show changes in surface features relative to the station.

[10] Figure 1 shows the geographical location of two RADARSAT image frames, from January 10 and 11, 1998. The SHEBA drift track is also shown, with the position on 11 January marked by a small dot (75°N, 150°E). Centered on that position are the two subimage frames, 40 × 40 km square and 200 × 200 km square. Figure 2 shows the SAR image of 11 January; the yellow box measures 40 × 40 km and is centered on the SHEBA station. Figure 3 shows the SAR image within that box; the station is at the center of the yellow circle. (The red and green grid lines are explained in section 2.2).

### 2.2. Ice Motion

[11] The RGPS, funded by NASA and developed at JPL, computes sea ice motion, deformation, and thickness through

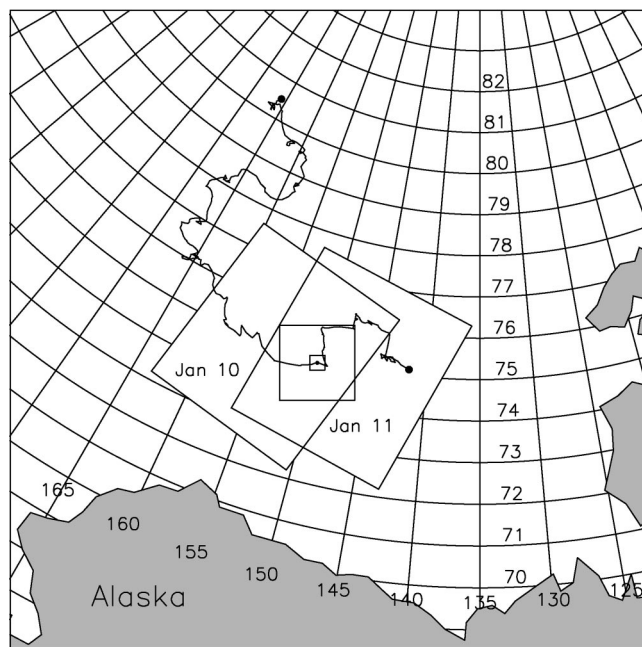


**Figure 1.** RADARSAT SAR image frames of 10 and 11 January 1998, illustrating the overlap that allows features in the first image to be tracked in the second image. The SHEBA drift track is also shown, with the position on 11 January marked by a small dot. Centered on the dot are two squares, 40 × 40 km and 200 × 200 km, showing the extent of the subimages that have been extracted from the original SAR image.

out the Arctic basin by following small Lagrangian cells in sequential RADARSAT SAR images [*Kwok et al., 1995*]. For the purposes of the SHEBA drift, the RGPS team at JPL created a special data set consisting of ice motion on a 5 km grid, 200 × 200 km in extent, and centered on the SHEBA station. The ice-tracking algorithm uses cross correlation to identify automatically common features in pairs of SAR images [*Kwok et al., 1990*]. The SHEBA ice motion data set is Eulerian: a new, regular 5 km grid is initialized on the first image of each sequential pair, and the grid points are tracked to the second image of the pair. A new grid is then initialized on that image for the purpose of tracking to the subsequent image. Particles of ice are not followed in a Lagrangian fashion through a long sequence of images. However, each newly initialized grid is centered on the SHEBA station as it drifts across the Arctic Ocean.

[12] There are 184 sets of ice motion data for the SHEBA drift, each one spanning (typically) a 1–3 day period. (The ice could not be tracked in every single pair of the 195 images.) The longest data gap is 16 days, from 25 December 1997 to 10 January 1998. The spatial extent of each ice motion product ranges from the full 200 × 200 km to only tens of kilometers in some summer cases where the tracking proved to be difficult because of surface features becoming “washed out.” Also, when the SHEBA station happened to fall within 100 km of the edge of an image, the full 200 × 200 km grid could not be tracked.

[13] There are two sources of errors in determining the ice motion from sequential images: geolocation errors and tracking errors [*Holt et al., 1992*]. The first refers to the uncertainty in the geographical location of each pixel. The second refers to

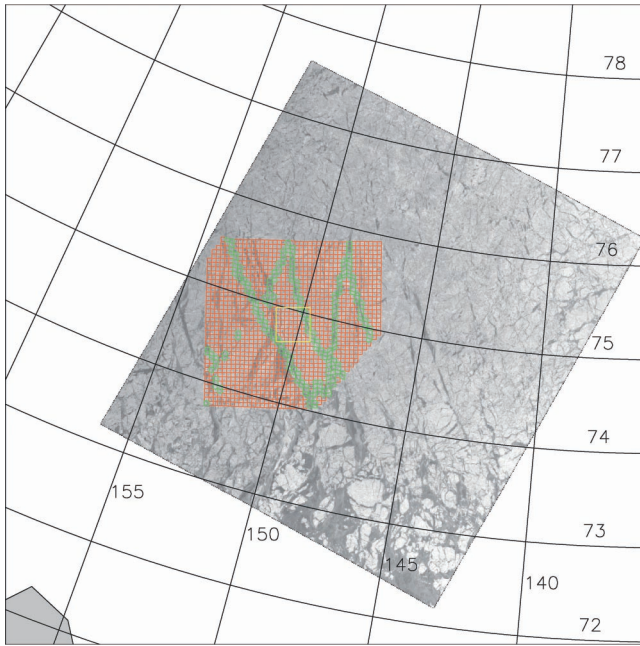


**Figure 2.** RADARSAT SAR image of 11 January 1998. The SHEBA station is at the center of the yellow box, which measures  $40 \times 40$  km. The grid illustrates the relative motion of the sea ice since the previous day. Red cells have remained rigid; green cells have deformed more than 15% ( $|\epsilon| > 0.15$ ). (Image copyright CSA 1998.)

the mistaken identification of corresponding pixels by the ice-tracking algorithm. These errors are uncorrelated with each other, and both are small in the present data set, on the order of 100–200 m. This leads to an uncertainty in each ice displacement vector of about 200 m (independent of the time interval over which the displacement occurs), which is at least as accurate as displacements obtained from drifting buoys [Lindsay *et al.*, 2000]. The uncertainty is much smaller than the mean displacement of 11 km for the 184 ice motion data sets. Only five of the 184 have a mean displacement less than 1 km.

[14] Ice motion fields are typically displayed with vectors. In Figure 2 we display instead the configuration of the grid on 11 January that originally consisted of regular 5 km squares on 10 January. Those grid cells that have remained square are shown in red. The ones that have deformed (by more than 15%) are shown in green. The pattern of deformation is discussed in section 3.2. Figure 3, the  $40 \times 40$  km subimage of 11 January, also shows the correspondence between the deforming (green) cells and certain leads in the SAR image.

### 2.3. Derived Products

[15] Knowledge of the ice motion on a regular grid allows one to estimate its spatial gradients, i.e., strain or strain rate. Let  $(u, v)$  represent the ice velocity at location  $(x, y)$ . We estimate  $u_x$  (partial derivative) and the other three partial derivatives for each 5 km cell using standard finite difference formulas. Values for individual cells can then be averaged together to obtain larger-scale strain rates, if desired. We combine these (whether averaged or not) into the strain rate invariants, divergence ( $D = u_x + v_y$ ) and shear ( $S = \sqrt{(u_x - v_y)^2 + (u_y + v_x)^2}$ ). The magnitude of the strain rate is given by  $|\epsilon| = \sqrt{D^2 + S^2}$ . The procedure is the same as that used by Stern *et al.* [1995] with ice motion data derived

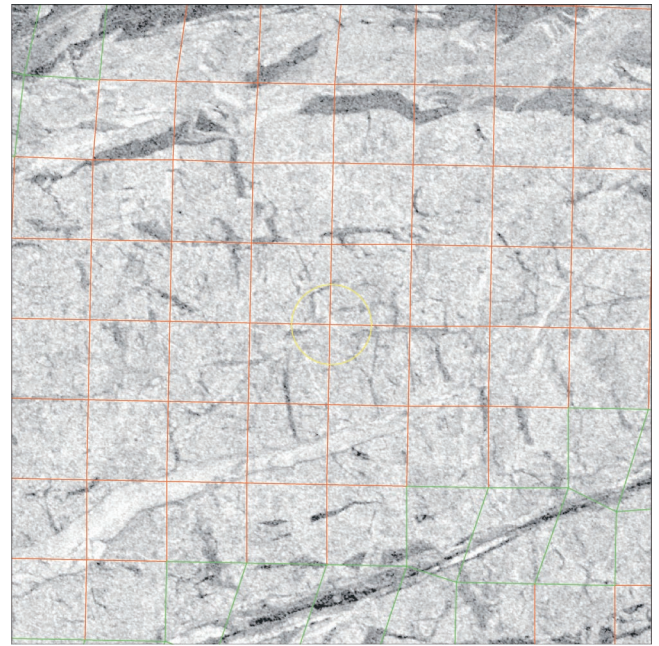


**Figure 3.** RADARSAT SAR subimage of the  $40 \times 40$  km region centered on the SHEBA station on 11 January 1998. This is a close-up of the yellow box in Figure 2. (Image copyright CSA, 1998.)

from ERS-1 SAR images by the predecessor of the RGPS. The result is a time series of 184 values of  $D$ ,  $S$ , and  $|\epsilon|$  (if strain rates have been spatially averaged) or 184 spatial patterns of  $D$ ,  $S$ , and  $|\epsilon|$  (if no spatial averaging). For example, Figure 4 shows the time series of ice divergence  $D$  in the vicinity of the SHEBA station, computed at four different spatial scales (averaging sizes) centered on the station. Figure 5 shows the spatial pattern of  $|\epsilon|$  over 12 time intervals in which each 5 km square is color-coded according to the size of  $|\epsilon|$ . These are discussed in section 3.2.

## 3. Kinematic Analysis

### 3.1. Ice Motion

[16] The dominant driving force on the sea ice is the wind. A complex regression of the year-long record of daily ice drift (from GPS) on the 10 m wind measured at the SHEBA station gives a squared correlation of 0.85, with the ice moving at 2% of the wind speed and  $29^\circ$  to the right of the wind vector. A seasonal analysis gives a squared correlation of 0.88 in winter, 0.79 in spring, and 0.92 in summer and fall.

[17] It is also known that the ice undergoes small inertial motions because of the rotation of the Earth. This can lead to aliasing of the ice velocity if the position of the ice is not measured over an integral number of inertial periods. Fortunately, the RADARSAT overpass time for 190 of the 195 images only varies by  $\pm 1$  hour (around 1800 UT), so the time intervals between images are close to multiples of the inertial period.

[18] Besides the general drift of the ice indicated by the trajectory in Figure 1, observations of ice motion from this data set (such as Figure 2) and other data sets clearly indicate that the winter ice cover consists of large rigid plates that move relative to one another along linear “cracks.” The value of the RGPS ice motion data sets is in the detailed spatial patterns of

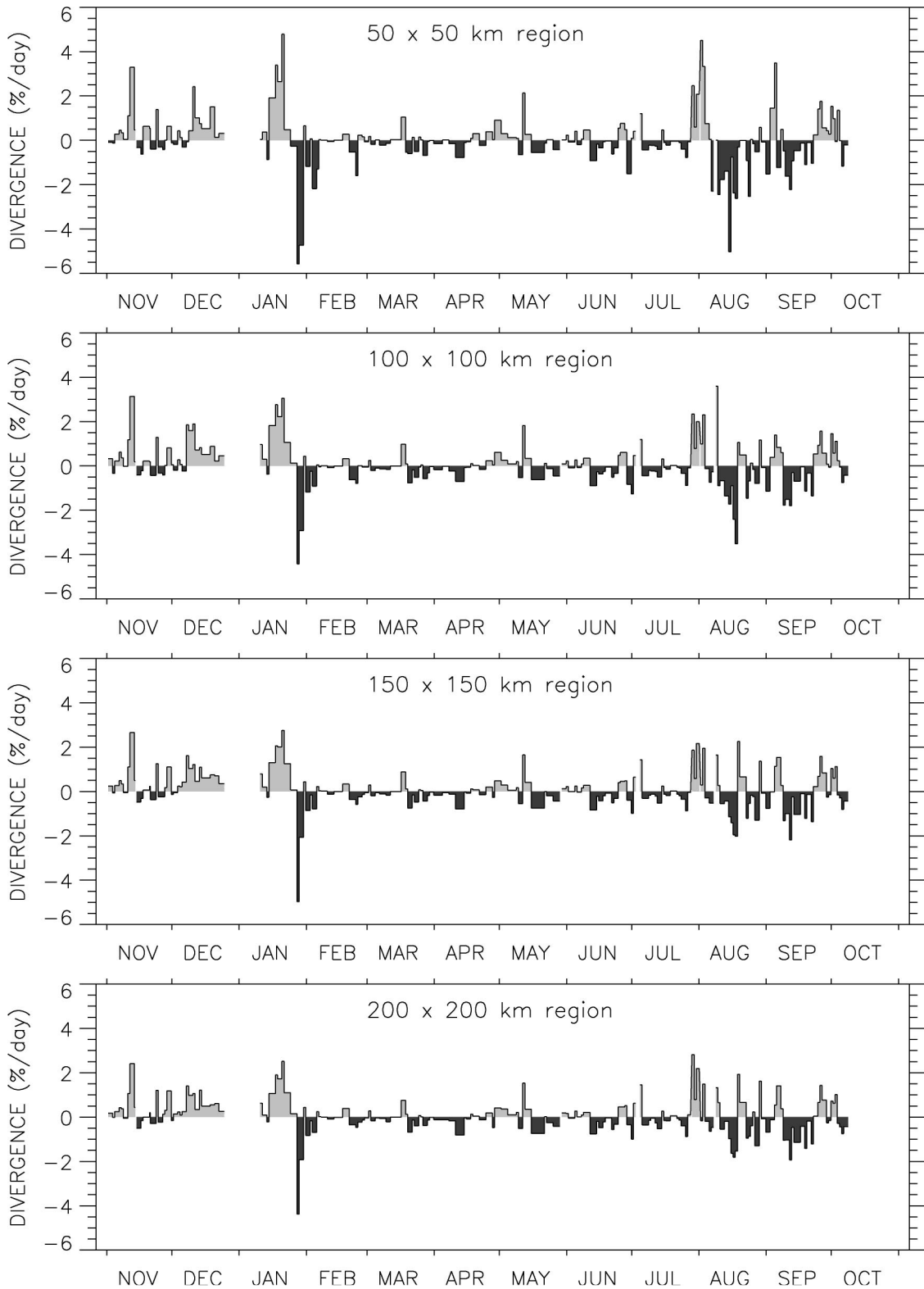


**Figure 4.** Time series of ice divergence in the vicinity of the SHEBA station computed at four different spatial scales (averaging sizes) centered on the station.

this differential ice motion, or deformation, around the SHEBA site.

**3.2. Ice Deformation**

[19] Sea ice deformation drives changes in the ice thickness distribution through the creation of leads, where new

ice can grow, and through the creation of pressure ridges, which contain more than one third of the mass of Arctic sea ice (according to both submarine ice draft data and a coupled ice-ocean model (Y. Yu and J. Zhang, unpublished manuscript, 2002)). Therefore characterizing the deforma-

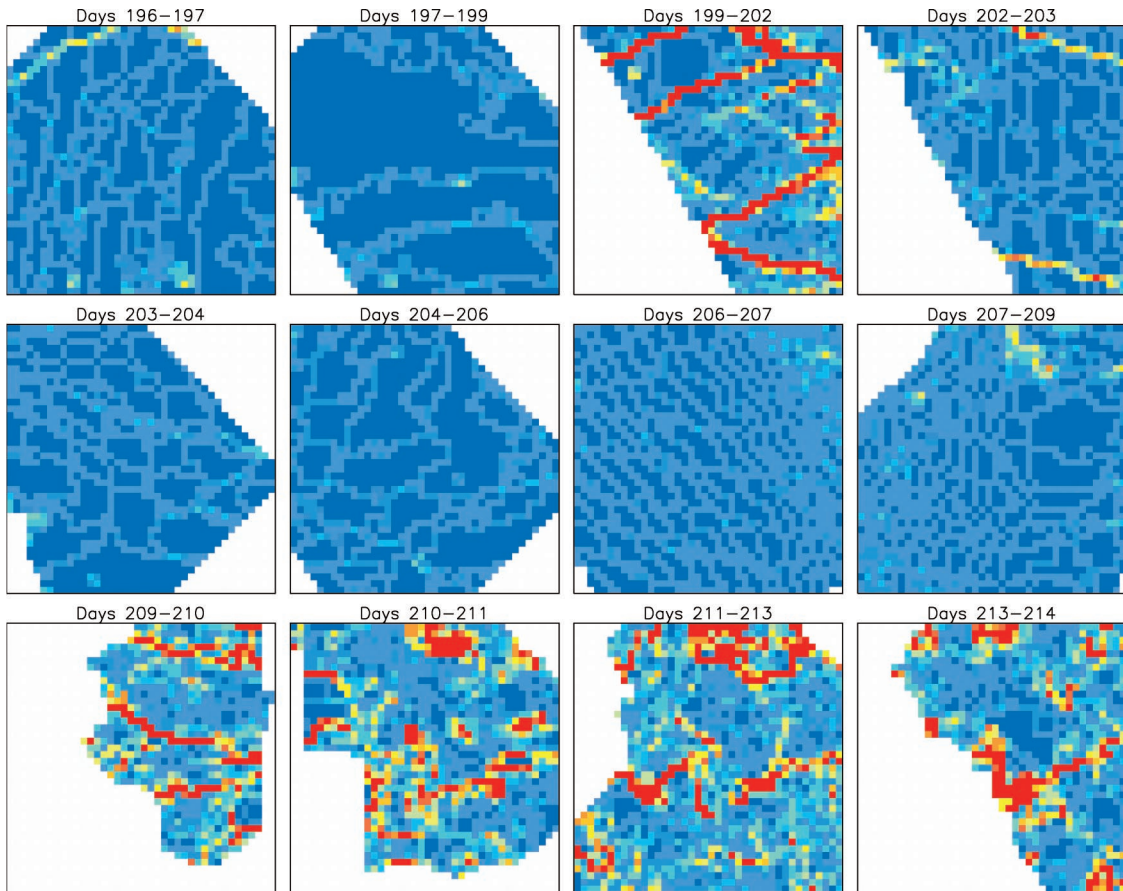


**Figure 5.** The spatial pattern of the magnitude of the ice strain  $|\epsilon|$  over 12 time intervals in the summer of 1998. Each panel is  $200 \times 200$  km in size, with the SHEBA station at the center. Each 5 km cell is color-coded according to  $|\epsilon|$  for that cell, from blue ( $|\epsilon| = 0$ ) through the spectrum to red ( $|\epsilon| > 0.25$ ). Day 196 is 15 July, and day 214 is 2 August.

tion is important for understanding the mass balance of the ice cover.

[20] The time series of ice divergence around the SHEBA site (Figure 4) shows an interesting annual cycle. In the fall and early winter, as the pack ice is growing and strengthening, the divergence is mainly positive (new leads form and new ice grows). All four spatial scales in Figure 4, from 50 to 200 km, indicate a cumulative divergence of about 25% between 1 November and 25 December. January contains large divergent and convergent events. Throughout most of the month the wind speed is moderate ( $\sim 5 \text{ m s}^{-1}$ ) and the direction varies from northerly to easterly. The ice drifts westward as leads form with a generally northwest-southeast orientation. At the end of January the wind speed picks up quickly ( $14 \text{ m s}^{-1}$  on 26 January) and the direction shifts to slightly south of easterly. This causes a large convergence of ice as the new leads that formed earlier in the month are forced to close and ridge [Richter-Menge *et al.*, 2002]. Then, from early February until the end of July, the divergent and convergent events are small, but the pack ice undergoes a gradual convergence of about 15% as the SHEBA station drifts within the Beaufort Gyre (see the surface air pressure patterns derived from drifting buoys by Rigor and Ormeyer [1999]). The gradual convergence persists beyond the onset of summer melt (29 May), which marks a thermodynamic change but not a dynamic change.

[21] Throughout June and July, as the air temperature hov-

ers around  $0^\circ\text{C}$ , the ice cover is melting and weakening. At the end of July a big storm blows through; the wind speed jumps from 4 to  $10 \text{ m s}^{-1}$  on 27–29 July, and the wind direction shifts from southerly to westerly. This gives rise to the large divergence seen in Figure 4 in late July and early August. It also marks a change in the character of the ice deformation. The winter pattern typically consists of large rigid areas of ice (plates) crossed by linear actively deforming zones (cracks), as in Figure 2. After 28 July, however, the nature of the deformation changes to a more random pattern consistent with free-drift conditions and low ice strength. Figure 5 illustrates the transition. The panels show the pattern of the magnitude of the ice strain  $|\epsilon|$  over 12 time intervals from days 196–197 (15–16 July) to days 213–214 (1–2 August). The SHEBA station is at the center of each  $200 \times 200$  km panel, and each 5 km cell is color-coded according to  $|\epsilon|$  for that cell, from blue ( $|\epsilon| = 0$ ) through the spectrum to red ( $|\epsilon| > 0.25$ ). The pattern of  $|\epsilon|$  for days 199–202 (18–21 July) shows winter characteristics: linear cracks (red) and plates (blue). This is followed by a week of almost no deformation activity, which ends with the storm of 28 July (day 209). The pattern of  $|\epsilon|$  after that date is markedly different (bottom four panels). The deforming zones are in clumps rather than in lines, and the distribution of  $|\epsilon|$  is more even, i.e., less dominated by purely rigid (blue) and highly deforming (red) cells. The amorphous character of the deformation pattern persists through 11 September and then

enters a 3 week transition period, after which it reacquires the winterlike properties of plates and linear cracks (not shown). This fall transition period coincides with a 3 week interval when the surface (2 m) air temperature goes through four oscillations between  $-2^{\circ}$  and  $-8^{\circ}\text{C}$  before plummeting to  $-22^{\circ}\text{C}$  on 4 October. Clearly, the leads and open water were gradually freezing up during the transition period, diminishing the freedom of the ice floes to drift independently. The pack ice became well consolidated by 4 October. The time series of divergence (Figure 4) allows the same interpretation: there are large excursions from the end of July to mid-September during free drift, followed by an apparent return to fall conditions (moderate positive divergence) after late September.

[22] The qualitative similarity between the four panels of Figure 4 suggests that the same events contributing to the divergence of the ice within 50 km of the SHEBA station also extend out to a scale of at least 200 km. The seasonal contributions to the divergence at the 100–200 km scale are roughly as follows: +25% in November and December, +5% in January, -15% from February through July, and -6% in late summer and early fall. This gives a net annual divergence on the order of +5%. However, at the 50 km scale the big convergent event in January dominates the divergent event, and the late summer convergence is also larger, so the net annual divergence is about -10%.

[23] The shear deformation  $S$  is much larger than the divergence  $D$ , as is usually the case. While the ice was diverging at about  $0.4\% \text{ d}^{-1}$  in the fall and early winter (all scales), the shear rate was  $\sim 2\% \text{ d}^{-1}$  at the 200 km scale and  $3\% \text{ d}^{-1}$  at the 50 km scale. The shear deformation peaked in January ( $4\text{--}6\% \text{ d}^{-1}$ ), was relatively low throughout the winter, spring, and early summer ( $\sim 1.5\% \text{ d}^{-1}$ ), and picked up again in late summer and early fall ( $3\text{--}4\% \text{ d}^{-1}$ ). During the cold season, shearing of the ice can create open water where new ice can grow [e.g., Stern *et al.*, 1995]. Thus shear deformation must be taken into account in modeling ice production and ridging.

## 4. Radiometric Analysis

### 4.1. Seasonal Characteristics

[24] The normalized radar cross section (“backscatter” or  $\sigma^0$ ) is the ratio of backscattered power to incident power at the target location, expressed either as a dimensionless ratio or in decibels ( $10 \log(\sigma^0)$ ). The backscatter from sea ice results from a combination of surface scattering and volume scattering, depending on such properties as the surface roughness and the brine volume. Dry snow is nearly transparent to C band (5.3 GHz) SAR, but the presence of even a small fraction of liquid water greatly diminishes the backscatter. A smooth surface such as calm water or new undeformed ice has a low backscatter, whereas wind-roughened water or deformed ice has a higher backscatter. See Hallikainen and Winebrenner [1992] for more details.

[25] The calibration accuracy of the RADARSAT ScanSAR imagery is described by Martyn *et al.* [1999]. The relative radiometric error within an image is 0.2 dB, and the relative error from image to image is 0.1 dB. The absolute radiometric error is 0.2 dB.

[26] Figure 6 illustrates the well-known linear relationship in SAR imagery between the mean backscatter and the standard deviation (both dimensionless). Each symbol represents one  $40 \times 40$  km subimage with a pixel size of 50 m, hence  $800 \times 800 = 640,000$  pixels. Before the mean and standard

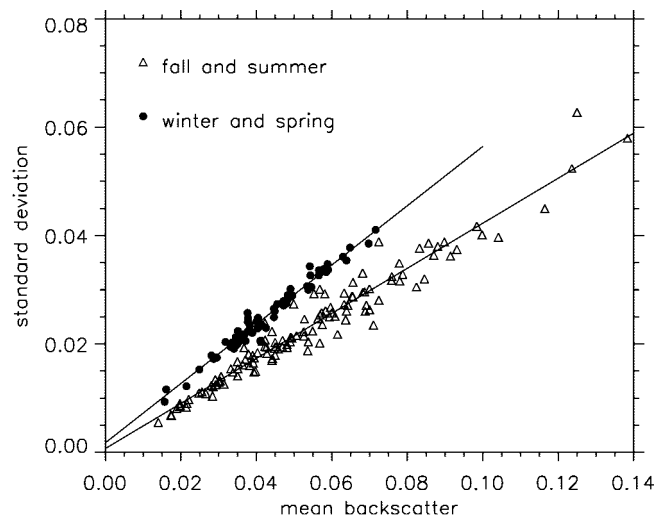


**Figure 6.** Standard deviation of backscatter versus mean backscatter (both dimensionless). Each symbol represents one  $40 \times 40$  km subimage. The slope of the linear relationship changes with season.

deviation are computed the central  $7 \times 7$  pixels containing the (high-backscatter) SHEBA station are deleted. In some cases the edge of the satellite swath cuts across the subimage, reducing the number of pixels with image data, but in only 12 cases is the number of pixels less than 600,000. The linear relationship between the mean and standard deviation changes with season: winter and spring (10 January to 7 June 1998) show a larger standard deviation relative to the mean than fall and summer (1 November to 25 December 1997 and 8 June to 8 October 1998). The slope of the line through the winter/spring points is 0.55 with squared correlation 0.97. The slope of the line through the fall and summer points is 0.42 with squared correlation 0.94. The different slopes could be due to different mixes of ice types (see section 4.2) that alter the average scattering properties of the ice.

[27] The backscatter from most surface types, including sea ice, generally decreases with increasing incidence angle. Figure 7 shows the relationship for the  $40 \times 40$  km subimages from fall (1 November to 25 December 1997) and winter/spring (10 January to 28 May 1998). For each subimage the center incidence angle (at the SHEBA station) is used. The slope of the line through the fall points is  $-0.14 \text{ dB deg}^{-1}$  with a squared correlation of 0.93. The slope of the line through the winter/spring points is  $-0.13 \text{ dB deg}^{-1}$  with a squared correlation of 0.92. The incidence angle across each full ScanSAR image (460 km wide) ranges from  $19^{\circ}$  to  $46^{\circ}$ , but within each 40 km wide subimage it varies by no more than  $\pm 1.2^{\circ}$  from the center value, which translates into  $\pm 0.17 \text{ dB}$  (using a slope of  $0.14 \text{ dB deg}^{-1}$ ). This is less than the relative radiometric error within an image; hence the incidence angle can be considered nearly constant within each 40 km subimage. The drop in backscatter from fall to winter/spring is due to a larger fraction of low-backscatter leads in winter/spring (see section 4.2), starting with the large divergent event in January (Figure 4).

[28] Figure 8 shows the mean backscatter versus time for the  $40 \times 40$  km subimages. The high-frequency variations are due to the incidence angle effect: if the SHEBA station happens to lie in the near range of the full ScanSAR image (closer to  $20^{\circ}$  incidence angle), then the backscatter within the subim-

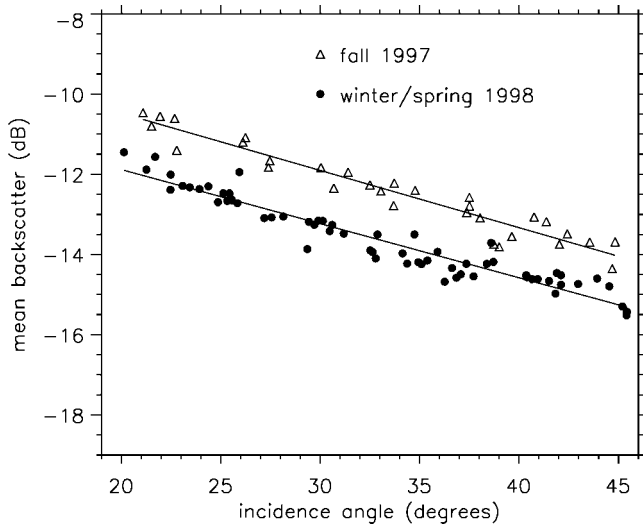


**Figure 7.** Mean backscatter versus incidence angle. Each symbol represents one  $40 \times 40$  km subimage. The drop in backscatter from fall to winter/spring is due to the changing mix of ice types within the 40 km image frames.

age is relatively high; if the SHEBA station lies in the far range (closer to the  $45^\circ$  incidence angle), then the backscatter is relatively low. The heavy line is not a running average; it is an adjustment of the mean backscatter to a standard incidence angle of  $32.5^\circ$ , using an adjustment factor (slope) of  $0.135 \text{ dB deg}^{-1}$ . Notice how stable the winter backscatter is: the temporal standard deviation of the 63 mean backscatter values from 10 January to 28 May is just 0.29 dB. *Kwok and Cunningham* [1994] noted the stability of the winter multiyear ice and first-year ice backscatter signatures in ERS-1 SAR images of the Beaufort Sea. The mean backscatter plotted in Figure 8 con-

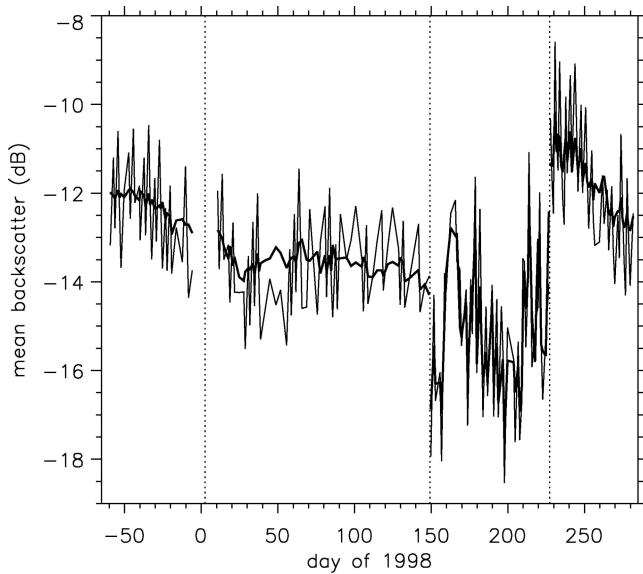


**Figure 8.** Mean backscatter versus time for the  $40 \times 40$  km subimages. The high-frequency variations are due to different incidence angles. The heavy line is an adjustment of the mean backscatter to a standard incidence angle of  $32.5^\circ$ . The mean winter backscatter is very stable compared to other seasons. Melt onset and freeze-up are marked by vertical dotted lines at 29 May (day 149) and 15 August (day 227).

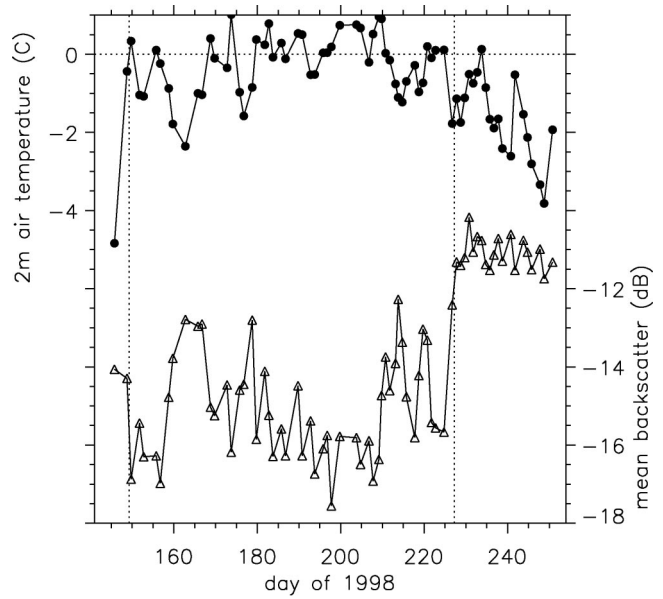


**Figure 9.** Daily 2 m air temperature interpolated to the SAR image times (upper curve, left scale) and mean backscatter (adjusted to  $32.5^\circ$  incidence angle, lower curve, right scale) versus time from 25 May (day 145) to 7 September (day 250). Melt onset and freeze-up are marked by vertical dotted lines at 29 May (day 149) and 15 August (day 227).

tains contributions from a variety of ice types, but multiyear ice is the dominant component, as we subsequently demonstrate.

[29] The onset of summer melt and fall freeze-up are evident in Figures 8 and 9 (dotted vertical lines at days 149 and 227). The 2 m air temperature in Figure 9 has been interpolated from daily values (obtained from the SHEBA Project Office) to the times of the SAR images. On 29 May (day 149) the air temperature rose above  $0^\circ\text{C}$  for the first time and rain fell. This saturated the surface with water, and the mean backscatter dropped by 2.5 dB in 1 day (compare to the gradual drop of 0.5 dB over the previous 2 months). On August 14 (day 226) the air temperature fell below  $-1^\circ\text{C}$ , and this triggered a jump of 4 dB in the mean backscatter (12–15 August) as the remaining liquid water on the surface froze. The temperature stayed below zero except for one brief excursion on August 22, and the mean backscatter stabilized at  $-11.5$  dB (Figure 9, lower curve, right scale). *Winebrenner et al.* [1994, 1996] used the changes in ERS-1 SAR backscatter of multiyear ice to make maps of the dates of melt onset and freeze-up in the Beaufort and Chukchi Seas. This technique can be used to measure the length of the melt season throughout the Arctic with RADARSAT SAR, and the RGPS will make such calculations.

[30] The backscatter is very sensitive to the presence of liquid water on the surface, which in turn is very sensitive to the fluctuations in air temperature around  $0^\circ\text{C}$ . In Figure 9 the dips in temperature around days 163, 177, 214, and 220 (14 June, 28 June, 2 August, and 8 August) are all accompanied by peaks in the backscatter of at least 2 dB above the background level. The correlation between air temperature and mean backscatter from 29 May (after melt onset) to 12 August (before freeze-up) is  $-0.57$ . The strong influence of the air temperature on the backscatter during the melt season explains why it is difficult or impossible to distinguish different ice types in the summer SAR imagery.

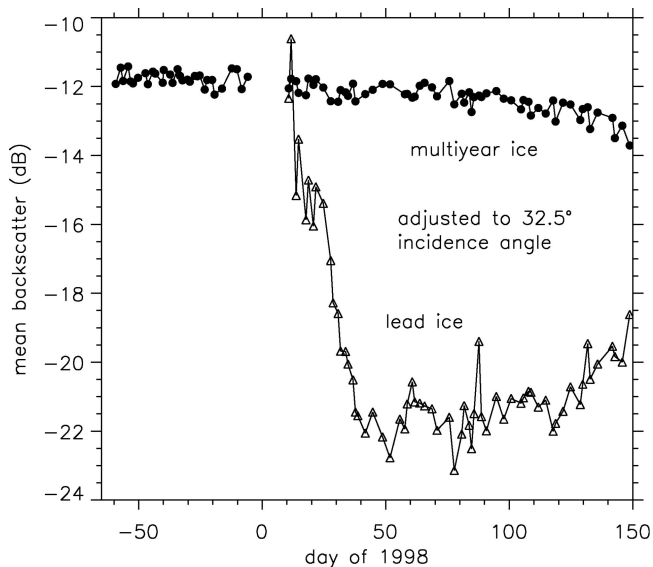


**Figure 10.** Mean backscatter (adjusted to  $32.5^\circ$  incidence angle) versus time following a patch of multiyear ice (circles) and lead ice (triangles). The two ice types are generally well separated, but lead ice can brighten briefly in the early stages of its formation, as on 10–11 January.

#### 4.2. Ice Types

[31] While each of the  $40 \times 40$  km subimages is centered on the SHEBA station as it drifts in the Arctic Ocean, the images are not strictly Lagrangian patches of sea ice; small amounts of ice are advected in and out of the 40 km frames over time, altering the mix of ice types and backscatter signatures. In order to follow the evolution of the same patches of ice over time we selected one region of multiyear ice and one region of lead ice that were clearly identifiable throughout the entire fall/winter/spring (for the multiyear ice) or winter/spring (for the lead ice). The multiyear patch contains about 4500 pixels and is located in Figure 3 about 7 km “left” (west) of the station location at the center; the lead ice patch contains about 500 pixels and is located about 7 km “right” (east) of the station. Figure 10 shows the time series of mean backscatter (adjusted to  $32.5^\circ$  incidence angle) for the two patches of ice. Although the backscatter of multiyear ice is relatively stable, it does decay at an increasing rate from January to the onset of melt at the end of May. The decay rate for January–March is about  $0.005 \text{ dB d}^{-1}$ , while the decay rate at the end of May approaches  $0.040 \text{ dB d}^{-1}$ . While it is likely that the final week of this decay is due to the rising temperature ( $-9^\circ$  to  $0^\circ\text{C}$  from 22 to 29 May) and hence rapidly changing dielectric properties of the ice, the earlier portion of the decay is not directly attributable to temperature effects. (One explanation might be a gradual decrease in the volume of scatterers in the bubbly upper layer of the ice as it ages.) The backscatter of the lead ice plotted in Figure 10 is even higher than that of the multiyear ice on 11 January (see Figure 3), but drops to  $-15 \text{ dB}$  on 13 January and then plummets to  $-21 \text{ dB}$  over the next 3 weeks. This illustrates both the large separation between first-year ice and multiyear ice that prevails most of the time and the potential for misclassification during the early stages of ice growth, when such phenomena as frost flowers can temporarily brighten the surface of a new lead [Nghiem *et al.*, 1997]. Notice that the decrease in the multiyear backscatter and the increase

in the first-year backscatter in the springtime are compensating trends that have a stabilizing effect on the mean backscatter (see Figure 8).

[32] The mean backscatter of multiyear ice in Figure 10 can be used as the basis of a simple classification procedure. First, we fit a quartic polynomial to the multiyear time series. This captures the long-term seasonal trend without any short-term fluctuations. Then we assign a threshold for multiyear ice by subtracting a constant “buffer” from the polynomial. Every pixel with backscatter above the threshold is classified as multiyear ice. What is the proper buffer to subtract? Clearly, the fraction of multiyear ice will increase as the buffer increases. The standard deviation of the multiyear backscatter is about 1.5 dB. Thus a buffer of 3 dB would set the threshold 2 standard deviations below the mean. The RGPS classification algorithm uses a buffer of 3.5 dB (R. Kwok, personal communication, 2000). In Figure 11 we plot the multiyear ice concentration (left scale) for three buffers: 3.0, 3.5, and 4.0 dB. The multiyear ice concentration starts at 94% (using the 3.5 dB buffer) in the fall (1 November), reaches a minimum of 61% at the end of January (see the large divergence in Figure 4), rebounds to 70% in early February, and then gradually increases back to 83% by the onset of melt (29 May). Of course, the SAR subimages that follow the SHEBA station are not true Lagrangian elements (as already noted): ice does advect in and out of the 40 km frames. In fact, using the RGPS ice motion data, we compute a net convergence of 12% at the 50 km scale from early February to the onset of melt, compared to an increase of 13% in the multiyear ice concentration over the same period. This suggests that multiyear ice advects into the 40 km image frames and replaces first-year ice as leads close.

[33] We also identified a region of open water or new ice in a lead that developed on 17, 18, 20, and 21 January. The mean backscatter in this 1000 pixel region ( $2.5 \text{ km}^2$ ) was between  $-23.4$  and  $-23.9 \text{ dB}$  (adjusted to  $32.5^\circ$  incidence angle) on all 4 days, with a standard deviation ranging from 0.5 to 2 dB. On the basis of these statistics we assigned pixels to the open water/new ice category if their backscatter was  $< -23 \text{ dB}$ . The lower curve in Figure 11 shows the concentration of open water/new ice (right scale). There is none to speak of in November and December, then a spike (5%) in middle to late January, and then a steady 1–2% for the rest of the winter and spring. The spike corresponds to the large divergence event in January (Figure 4) and the dip in multiyear ice concentration (upper curves). Since new ice may develop frost flowers that increase its radar backscatter, the open water/new ice category must be interpreted as the area of very recent openings in the pack ice. This is a subset of “leads,” whose identification depends on shape as well as backscatter. To complete the classification of ice types, ice that is brighter than  $-23 \text{ dB}$  but darker than multiyear ice goes into the “first-year ice” category.

## 5. Conclusions

[34] We have described and analyzed a unique data set consisting of a time series of 195 high-resolution RADARSAT SAR images centered on the SHEBA station plus the associated ice motion data on a 5 km grid computed by RGPS, spanning the period from 1 November 1997 to 8 October 1998.

[35] Analysis of the ice deformation shows a clear distinction between winter and summer conditions. Winter is characterized by linear intersecting zones of high deformation (active cracks) separating plates of rigid ice. Summer is

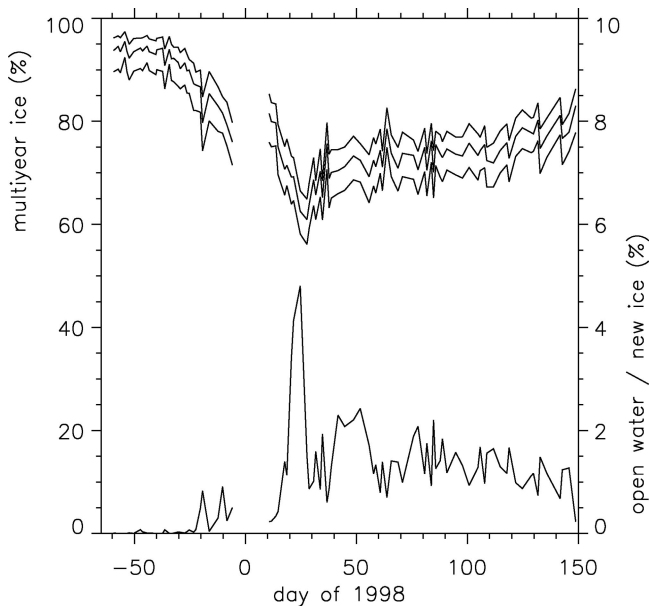


**Figure 11.** Multiyear ice concentration (upper curves, left scale) for three different thresholds and open water/new ice concentration (lower curve, right scale). The SAR subimages that follow the SHEBA station are not true Lagrangian elements: ice does advect in and out of the 40 km frames, so the concentration of multiyear ice is not constant.

characterized by a more random pattern of deformation due to free drift and low ice strength. The transition from winter to summer conditions occurred abruptly at the end of July in response to a strong storm, after the ice had been melting and weakening for 2 months. The transition back to winter conditions occurred more gradually from mid-September to early October, as the ice slowly consolidated with dropping temperature. Thus the “kinematic” summer started 2 months after the thermodynamic summer and ended a month and a half after it.

[36] The time series of radar backscatter also shows seasonal transitions. The backscatter is stable in the fall and early winter (November–December 1997) with 90% or higher multiyear ice concentration. The backscatter drops slightly in January because of the opening of large leads and is then very stable throughout the rest of the winter and spring. The onset of melt (29 May) brings a large drop in the mean backscatter as water in the surface layer obliterates the distinction between ice types in the SAR imagery. The summer signature is strongly affected by the presence of water on the surface and so fluctuates with the cycles of freezing and thawing. The backscatter jumps abruptly on 14–15 August, signaling the start of fall freeze-up. Multiyear ice, first-year ice, and open water/new ice can be distinguished in fall/winter/spring but not during the summer melt season.

[37] Future work with the data sets described here will focus on tying together the kinematics and the radiometry more closely. In addition, the RGPS at the Alaska SAR Facility is currently turning out data products for the SHEBA year that consist of ice deformation and thickness (the thin end of the distribution) for the entire western Arctic. This should prove to be a rich data set for SHEBA investigators.

[38] **Acknowledgments.** We thank the Alaska SAR Facility in Fairbanks for providing the RADARSAT SAR imagery and the cali-

bration software. We thank Ron Kwok and the RGPS team at JPL for creating the special ice motion data set for SHEBA. We also thank two anonymous reviewers for their comments. The meteorological data are courtesy of the SHEBA Project Office. This work was performed under grant OPP9720144 from the National Science Foundation in support of the SHEBA Project Office at the University of Washington.

## References

- Babko, O., Rafting in mechanical redistribution of sea-ice thickness, M. S. thesis, Univ. of Wash., Seattle, 2000.
- Curry, J. A., J. L. Schramm, D. Perovich, and J. O. Pinto, Applications of SHEBA/FIRE data to evaluation of snow/ice albedo parameterizations, *J. Geophys. Res.*, *106*, 15,345–15,355, 2001.
- Hallikainen, M., and D. P. Winebrenner, The physical basis for sea ice remote sensing, in *Microwave Remote Sensing of Sea Ice*, *Geophys. Monogr. Ser.*, vol. 68, edited by D. Carsey pp. 29–46, AGU, Washington, D.C., 1992.
- Hibler, W. D., III, and E. M. Schulson, On modeling the anisotropic failure and flow of flawed sea ice, *J. Geophys. Res.*, *105*, 17,105–17,120, 2000.
- Holt, B., D. A. Rothrock, and R. Kwok, Determination of sea ice motion from satellite images, in *Microwave Remote Sensing of Sea Ice*, *Geophys. Monogr. Ser.*, vol. 68, edited by F. D. Carsey, pp. 343–351 AGU, Washington, D. C., 1992.
- Hopkins, M. A., A granular sea ice model, in *Proceedings of the 15th International Conference on Port and Ocean Engineering Under Arctic Conditions*, vol. 1, edited by J. Tuhkuri and K. Riska, pp. 91–96, Tummavuoren Kirjapaino Oy, Vantaa, Finland, 1999.
- Kerman, B., P. Wadhams, N. Davis, and J. Comiso, Informational equivalence between synthetic aperture radar imagery and the thickness of Arctic pack ice, *J. Geophys. Res.*, *104*, 29,721–29,731, 1999.
- Kwok, R., and G. F. Cunningham, Backscatter characteristics of the winter ice cover in the Beaufort Sea, *J. Geophys. Res.*, *99*, 7787–7802, 1994.
- Kwok, R., J. C. Curlander, R. McConnell, and S. S. Pang, An ice-motion tracking system at the Alaska SAR facility, *IEEE J. Oceanic Eng.*, *15*, 44–54, 1990.
- Kwok, R., E. Rignot, B. Holt, and R. Onstott, Identification of sea ice types in spaceborne synthetic aperture radar data, *J. Geophys. Res.*, *97*, 2391–2402, 1992.
- Kwok, R., D. A. Rothrock, H. L. Stern, and G. F. Cunningham, Determination of the age distribution of sea ice from Lagrangian observations of ice motion, *IEEE Trans. Geosci. Remote Sens.*, *33*, 392–400, 1995.
- Lindsay, R. W., Ice deformation near SHEBA, *J. Geophys. Res.*, AO 1029/2000JC000445, in press, 2002.
- Lindsay, R. W., Y. Yu, H. L. Stern, D. A. Rothrock, and R. Kwok, RADARSAT geophysical processor system products: Evaluation and validation, report, Appl. Phys. Lab., Univ. of Wash., Seattle, 2000.
- Martyn, P., J. Williams, J. Nicoll, R. Guritz, and T. Bicknell, Calibration of the RADARSAT SWB processor at the Alaska SAR facility, paper presented at IEEE International Geoscience and Remote Sensing Symposium (IGARSS '99), Inst. of Electr. and Electr. Eng., Hamburg, Germany, 1999.
- Moritz, R. E., and D. K. Perovich (Eds.), Surface heat budget of the Arctic Ocean Science Plan, *ARCSS/OAII Rep. 5*, 64 pp., Univ. of Wash. Seattle, 1996.
- Moritz, R. E., and H. L. Stern, Relationships between geostrophic winds, ice strain rates and the piecewise rigid motions of pack ice, in *Solid Mechanics and Its Applications*, vol. 94, *IUTAM Symposium of Scaling Laws in Ice Mechanics and Ice Dynamics*, edited by J. P. Dempsey and H. H. Shen, pp. 335–348, Kluwer Acad., Norwell, Mass., 2001.
- Nghiem, S. V., S. Martin, D. K. Perovich, R. Kwok, R. Drucker, and A. J. Gow, A laboratory study of the effect of frost flowers on C band radar backscatter from sea ice, *J. Geophys. Res.*, *102*, 3357–3370, 1997.
- Richter-Menge, J. A., S. L. McNutt, and J. E. Overland, Relating Arctic pack ice stress and deformation under winter conditions, *J. Geophys. Res.*, 10.1029/2000JL00087, in press, 2002.
- Rigor, I., and M. Ortmeyer, Observations of sea level pressure, surface air temperature and ice motion from the International Arctic Buoy Programme, *Tech. Rep. 9902*, Appl. Phys. Lab. Univ. of Wash., Seattle, 1999.

- Stern, H. L., D. A. Rothrock, and R. Kwok, Open water production in Arctic sea ice: Satellite measurements and model parameterizations, *J. Geophys. Res.*, *100*, 20,601–20,612, 1995.
- Winebrenner, D. P., E. D. Nelson, R. Colony, and R. D. West, Observation of melt onset on multiyear Arctic sea ice using the ERS1 synthetic aperture radar, *J. Geophys. Res.*, *99*, 22,425–22,441, 1994.
- Winebrenner, D. P., B. Holt, and E. D. Nelson, Observation of autumn freeze-up in the Beaufort and Chukchi Seas using the ERS 1 synthetic aperture radar, *J. Geophys. Res.*, *101*, 16,401–16,419, 1996.
- 
- R. E. Moritz and H. L. Stern, Polar Science Center, Applied Physics Laboratory, University of Washington, 1013 NE 40th Street, Seattle, WA 98105–6698, USA. (harry@apl.washington.edu)